Arranz, G.; Flores, O.; García-Villalba, M. (2020) Three-dimensional effects on the aerodynamic performance of flapping wings in tandem configuration, *Journal of Fluids and Structures*, v. 94, 102893, pp.: 1-16.

Three-dimensional effects on the aerodynamic performance of flapping wings in tandem configuration

G. Arranz, O. Flores, M. García-Villalba

Abstract

Direct numerical simulations have been performed to analyse how three-dimensional effects influence the performance of wings in tandem configuration undergoing a two-dimensional optimal kinematics. This optimal motion is a combination of heaving and pitching of the airfoils in a uniform free-stream at a Reynolds number $Re = 1000$ and Strouhal number $St_c = 0.7$. Wings of two different aspect ratios, $\mathit{R} = 2$ and 4, undergoing the 2D motion have been considered. It has been found that the interactions between the vortical structures of the fore- and the hind-wings are qualitatively similar to the two-dimensional case for both R. However, the ratio between the mean thrust of the hind-wing and the fore-wing decreases from 80% in 2D to 70% in 3D, implying that the 3D effects are detrimental for the vortical interactions between the wings in terms of thrust production. Nonetheless, the propulsive efficiency remains constant both in 2D and 3D, for both R. A more realistic flapping motion has also been analysed and compared to the heaving motion. It has been found that the aerodynamic forces decrease when the wings are in flapping motion. This detrimental behaviour has been linked to a sub-optimal motion of the inboard region of the wings. This sub-optimal region of the wings entails a decrease of the mean thrust and of the propulsive efficiency compared to the heaving case, which are more pronounced for the $\mathit{R} = 4$ wings.

1 Introduction

In contrast to birds, bats and most insects, dragonflies have two pairs of wings which can be controlled independently [1, 2]. By modifying the kinematics and the phase relationship between the fore and hind pair of wings, dragonflies are capable of performing rapid manoeuvres, accelerate, or cruising efficiently [3, 4]. This versatility, and the recent interest in the development of micro air vehicles (MAVs), have fostered the scientific community to understand which are the mechanisms that govern the flight of these insects. Thanks to this interest, it has been discovered, and now it is widely accepted, that one of the most important mechanisms dragonflies take advantage of is the wake interaction between their wings [5, 6, 7].

In hovering flight, the wake interaction between the fore- and the hind-wing has a negative effect in terms of lift generation. This was shown by Maybury and Lehmann [8]. They conducted experiments on two robotic flapping wings vertically stacked, showing that the total vertical force obtained was reduced due to the interaction between the wings, regardless of the phase shift of the wings. Likewise, Wang and Sun [9] performed numerical simulations of two wings in tandem configuration with a motion close to the actual motion of dragonfly's wings. By modifying the phase shift between the wings, they showed that the vertical force developed by each wing is always lower than the force developed by the same wing when isolated. Similar results were obtained by Rival *et. al* [10] for two-dimensional pitching and heaving plates. Nonetheless, they found that for an optimal phase shift, similar values of mean lift than the foils when isolated were achieved, but with more constant force production over the cycle. Likewise, Wang and Russel [5] performed numerical simulations of the two-dimensional wings' motion of a dragonfly, revealing that counter-stroking of the wings minimizes the aerodynamic power. Later, Usherwood and Lehmann [7] found that adequate wing phasing during hovering can lead to a power reduction up to 22% compared with a single pair of wings.

Contrary to hovering, airfoil tandem configurations in forward flight can outperform isolated airfoils in terms of aerodynamic force production or propulsive efficiency. By modifying only the phase lag between two airfoils in tandem under a simplified pitching/heaving motion, Broering and Lian [11] were able to obtain higher lift or propulsive efficiency compared to a single airfoil. Likewise, Boschistch *et al.* [12] performed a parametric study of the phase lag and spacing between two pure pitching foils. They observed a banded pattern of the thrust and propulsive efficiency in the phase-spacing diagram,

revealing a linear dependency between both parameters. This dependency was later observed for combined pitching/heaving foils [13, 14], and it was also mentioned by Maybury and Lehmann [8] for 3D wings in hovering configuration. Kamisava and Isogai [15] performed numerical simulations to find the flapping kinematics of two pairs of flapping tandem wings of minimum required power for forward flight. They found that, for the range of velocities studied, the required power was lower than the maximum available power. More recently, Nagai *et al.* [16] studied the effect of phasing of tandem flapping wings in forward flight. Their results suggest that actual dragonfly might not select the phase differences in term of aerodynamic efficiency but also in terms of other factors such as longitudinal manoeuvrability or flight stability.

Other studies have focused on finding optimal tandem kinematics in two dimensions [17, 18, 19]. However, there are fewer studies addressing the aerodynamic performance of optimal kinematics in 3D wings, specially in terms of comparison with their corresponding 2D configurations. There are only a few works that compare 2D and 3D configurations with the same kinematics, which are briefly reviewed next.

Zheng *et al.* [20] analysed the forewing-hindwing interaction of finite aspect ratio wings in heaving and pitching motion. Their results revealed discrepancies with past 2D studies undergoing similar kinematics, which might be attributed to 3D effects. However, flow visualization was limited by phase-locked 2D measurements at a single spanwise location, leaving as an open question if three dimensional effects significantly affect the forewing-hindwing interaction. Kurt and Moored [21] experimentally analysed the effect of the wing tip vortices of two tandem wings of $Æ = 2$ in pure pitching motion on the propulsive efficiency and thrust. To do so, they measured the forces on the wings for a range of different phasing and spacing, and repeated the experiments placing a splitter plate and a surface plate at the wing tips to minimize 3D effects. Their results show many broad similarities between both configurations; however, they found that, for the 3D configuration, increasing the spacing while keeping the phase lag constant, always results in a decrease of the propulsive efficiency due to the breakdown of the vortices. On the contrary, when 3D effects were minimized, optimal configurations were found for larger spacing between the wings. A comparison between two tandem airfoils in heaving and pitching motion and two wings of $Æ = 2$ under the same kinematics and spacing was performed by Broering and Lian [11] by means of numerical simulations. They compared the 2D and 3D simulations for 3 different phases. Generally, three dimensional effects led to a force reduction; nonetheless, collective propulsive efficiencies for the three-dimensional cases were very similar or even slightly higher than their two-dimensional counterparts. Overall, these works show a discrepancy on the extent of the influence that the 3D effects have on the aerodynamic performance of a two-dimensional (2D) configuration.

Moreover, it should be noted that previous comparisons between 2D and 3D configurations, [11, 21], consider the motion of the finite wings to be two-dimensional (i.e., heaving). However, actual motion of dragonfly's wings is a flapping motion in which each section of the wing has a different velocity. Practically no studies are found in the literature which compare flapping kinematics with a 2D motion. Sun and Lan [22] performed a numerical simulation of a pair of dragonfly tandem undergoing a realistic hovering motion, and compared the obtained aerodynamic forces with those of a 2D computation based on similar wing kinematics; They observed that, for the particular configuration, 3D fore-hind wing interaction is weaker than 2D interaction in terms of force generation. Nonetheless, we have not found in the literature other studies which assessed the effect of implementing a 2D optimal kinematics in a 3D configuration with flapping motion. Therefore, the objective of the present study is to analyse how three dimensional effects influence the aerodynamic forces and flow structures of tandem wings with a flapping motion. To that end, we perform direct numerical simulations (DNS) of tandem wings in flapping motion, tandem wings in heaving motion and tandem airfoils (2D) in heaving motion. Moreover, in this study we analyse the effect of the $Æ$ by considering wings of $AR = 2$ and 4, extending the results from [11, 20, 21] which only considered a single $Æ$.

The structure of the paper is as follows: the description of the problem and computational set-up is provided in section 2; the discussion of the results from the simulations is given in section 3; and section 4 gathers the main conclusions extracted from this study.

2 Methodology

2.1 Problem description

Two equal, finite wings in an in-line tandem arrangement and immersed in a uniform and constant free-stream of magnitude U, are considered. Both wings move with a kinematics based on the optimal, two-dimensional configuration of Ortega-Casanova & Fernández-Feria [18]. The motion corresponds to a combination of heaving and pitching about the mid chord. The pitching angle, θ, and heaving amplitude, h, are described by the sinusoidal functions:

$$h_i(t) = h_0 \cos\left(2\pi f t + \varphi_{h,i}\right), \tag{1}$$

$$\theta_i(t) = \theta_0 \cos\left(2\pi f t + \varphi_{\theta,i}\right), \tag{2}$$

where the subscript i indicates the wing ($i = 1$ fore-wing, $i = 2$ hind-wing) as shown in Figure 1. In eqs. (1) and (2), h_0 is the maximum heaving amplitude, θ_0 is the pitching amplitude, f is the frequency, $\varphi_{h,i}$ is the heaving phase shift and $\varphi_{\theta,i}$ is the pitching phase shift. The frequency and heaving amplitude are fixed by the non-dimensional numbers, $St_c = fc/U$ and $St_a = h_0 f/U$. All the parameters that define the motion are gathered in Table 1. Note that, according to the values of $\varphi_{h,i}$ and $\varphi_{\theta,i}$ in Table 1, pitching is advanced $3\pi/4$ with respect to heaving for both foils. Consequently, the motion of both foils is identical with a phase shift equal to π. Moreover, since the pitch angle averaged over a cycle is zero, the motion is symmetric with respect to the horizontal plane.
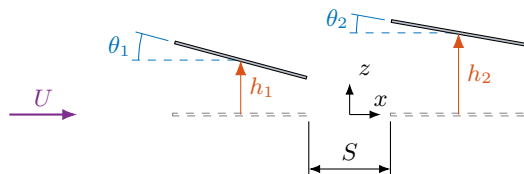

Figure 1. Sketch of the 2D-kinematics with the definition of θ_i and h_i. The inertial reference frame is also depicted for reference.

i	$\varphi_{h,i}$	$\varphi_{\theta,i}$	θ_0	St_c	St_a
1	0	$3\pi/4$	25°	0.7	0.17
2	π	$-\pi/4$			

Table 1. Kinematic parameters of the two-dimensional configuration.

The airfoil sections correspond to a flat plate with chord, c. The distance between the trailing edge of the fore-wing and the leading edge of the hind-wing when they lay onto a horizontal plane is $S/c = 0.5$ (see Figure 1). The Reynolds number based on the chord and the free-stream velocity is $Re = Uc/\nu = 1000$ for all the cases.

For the three-dimensional simulations, wings of rectangular planform with span, b, and the same cross-section as the 2D airfoils are considered. We study two aspect ratios, $Æ = b/c = 2$ and 4, and two kind of motions: heaving and flapping (i.e., rotation about an axis parallel to the free-stream velocity). Kinematics of the finite span wings in the heaving case is straightforward: all chordwise sections of the wings move according to eqs. (1) and (2), exactly as in the 2D case. On the contrary, in flapping motion, only one chordwise section has the same vertical amplitude, h_0, as in the 2D case. We denote this section as the *characteristic section*, and set it to be at $0.65b$ from the inboard wing tip. Moreover, the axis of rotation for the flapping motion is located at a fixed distance to the inboard wing tip, set to $\Delta\xi = c$ for all flapping cases. For clarity, Figures 2a and 2b show a sketch of the wings in flapping motion, the position of the characteristic section, and the position an orientation of the flapping axis. The figures also include the wing-fixed reference frames, Σ_i. For the i-wing, the origin of Σ_i is located at the mid-chord of the inboard wing tip, the ξ_i-axis is oriented along the spanwise direction and coincides with the pitching axis, the η_i-axis is perpendicular to the wing surface, and τ_i-axis correspond to the chordwise direction.

As shown in Figure 2b, the flapping motion of the wings depends on the vertical amplitude of the characteristic section, h_0, the distance of this section to the inboard wing tip, ξ_C, and the root offset, $\Delta\xi$. Hence, the flapping angle (see Figure 2a) is:

$$\phi_i(t) = \phi_0 \cos\left(2\pi f t + \varphi_{h,i}\right), \tag{3}$$

where $\phi_0 = \sin^{-1}\left(h_0/(\Delta\xi + \xi_C)\right)$ is the flapping amplitude. For the aspect ratios considered here, $\phi_0 \approx 6.1°$ and 3.9° for $Æ = 2$ and 4, respectively. On the other hand, the pitching axis coincides with the longitudinal symmetry axis of the wing, as shown in Figure 2a. Finally, it should be pointed out that the wing reference frames defined in Figure 2a are also used when the wings are in heaving motion to ease the comparison between the cases.
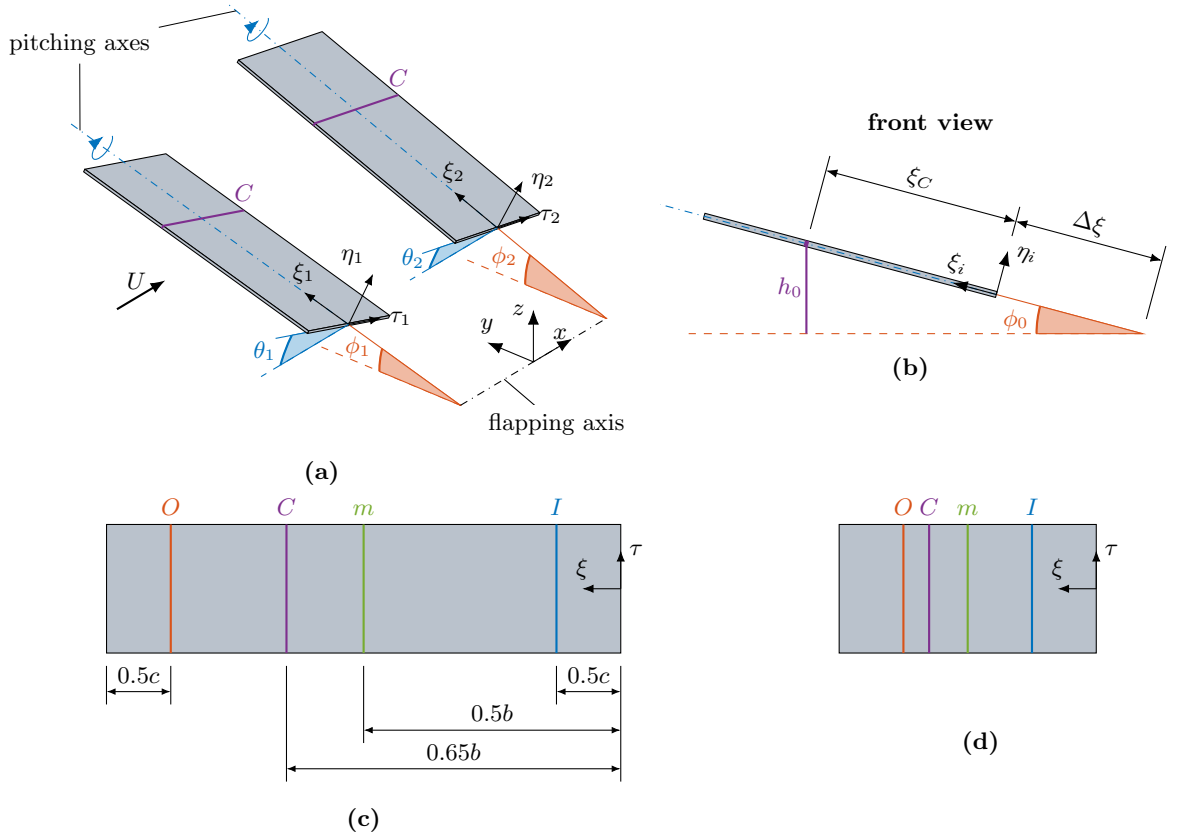
3

Figure 2. (a) Sketch of the flapping motion. The sections whose heaving amplitude is h_0 are highlighted in purple. The inertial reference frame $\Sigma \equiv (x, y, z)$ and the body reference frames $\Sigma_i \equiv (\tau_i, \xi_i, \eta_i)$ are also shown. (b) Front view of a single wing with the definition of $\Delta\xi$ and ξ_C. (c) Illustration of the chordwise sections where the sectional forces are computed for $\mathcal{R} = 4$ and (d) $\mathcal{R} = 2$.

In the subsequent sections, the aerodynamic forces at certain chordwise sections are analysed. These sections are sketched in Figures 2c and 2d: section m corresponds to the wing section at the midspan; sections I and O are located at $0.5c$ from the inboard and outboard wing tips, respectively (note that, in the heaving case, the forces at both sections will be the same owing to symmetry); and section C corresponds to the characteristic section defined above.

2.2 Computational set-up

Direct numerical simulations (DNS) are performed with the in-house code TUCAN, which solves the Navier-Stokes equations of the incompressible flow. TUCAN uses second-order finite differences for the spatial discretization in a staggered grid and a 3-stage, low-storage Runge-Kutta scheme for time integration. The time step is always selected so that the Courant–Friedrichs–Lewy number is smaller than 0.2. The presence of the bodies is modelled by means of the immersed boundary method proposed by Uhlmann [23]. The present algorithm has been successfully used for the simulation of aerodynamic flows, both in two- [24, 25] and three-dimensions [26, 27, 28, 29, 30].

The computational domain is a rectangular prism, displayed in Figure 3. The wings are centered in a refined region ($3.5c \times L_{y_r} \times L_{z_r}$ in Figure 3) with a uniform grid spacing in all directions, $\Delta r = c/96$. Outside this region, a constant stretching of 1% is applied to the grid in all directions. The dimensions of the refined region depend on the $\mathcal{R}$ and on the motion of the wings. For the heaving motion, $L_{y_r}/c = 1 + \mathcal{R}$ and $L_{z_r}/c = 1$. For the flapping motion, $L_{y_r}/c = 1 + \mathcal{R}$ and $L_{z_r}/c = 1.6$ and 2, for $\mathcal{R} = 2$ and 4, respectively. Finally, $L_{y_i} = 3c$ in the heaving case and $L_{y_i} = 0.5c$ in the flapping cases. Thus, in flapping motion the plane $Y = 0$ contains the flapping axis. As a result, the 3D simulations consists of around 2×10^8 grid points, depending on the particular case. The computational domain for the 2D simulation corresponds to a $Y = const.$ plane of the 3D computational domain with a uniform grid spacing $\Delta r = c/96$, leading to a grid with 9×10^5 points.

In terms of boundary conditions, a uniform free-stream velocity, U, is imposed at the inflow plane ($X = 0$). A convective boundary condition is imposed at the outflow plane ($X = 14c$). Free-slip
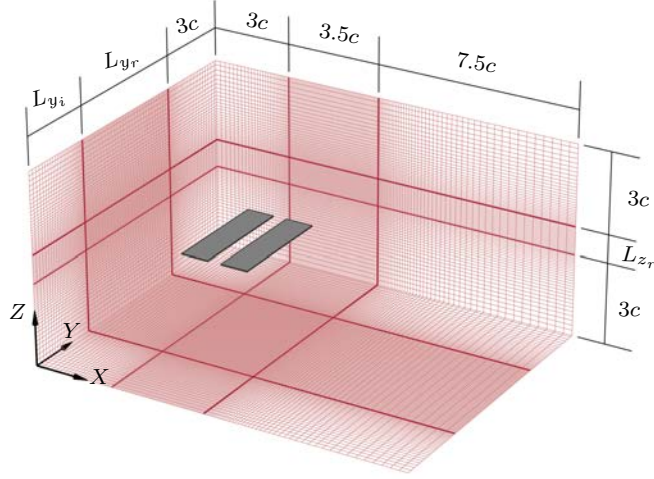
4

Figure 3. Sketch of the 3D computational domain. Solid lines delimit the uniform grid and the stretched grid. Only one of each five grid lines is represented.
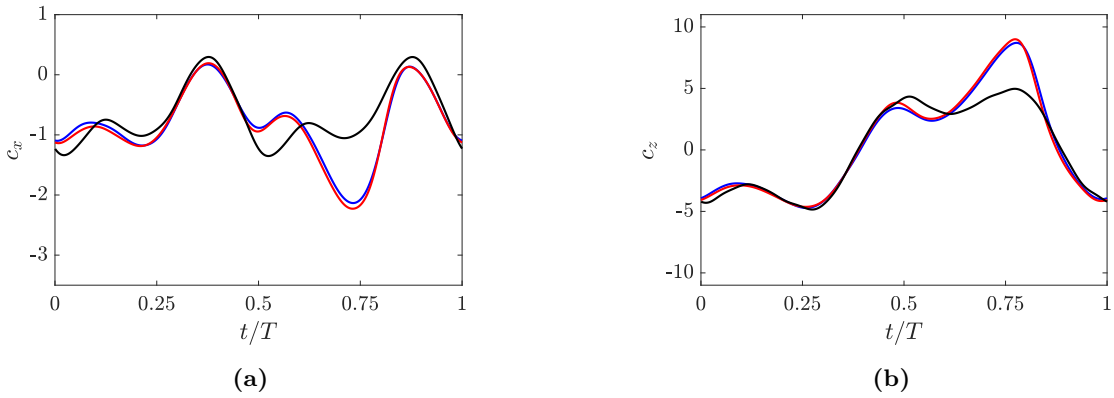

Figure 4. Temporal evolution of the (a) horizontal and (b) vertical force coefficients of the hind airfoil. (——) $\Delta r = c/48$; (——) $\Delta r = c/96$; and (——) $\Delta r = c/192$.

boundary conditions are imposed at the lateral boundaries.

TUCAN uses and immersed boundary method, which requires the specification of a Lagrangian mesh for the wings. Since the wings are flat plates, two flat surfaces are employed to discretize each wing. A uniform grid is used in each surface, with a grid spacing $\Delta r = c/96$ in both spanwinse and chordwise directions. The two surfaces discretizing each wing are separated a distance Δr, leading to a thickness $e/c \approx 0.01$.

The grid resolution reported in the previous paragraphs was selected after performing a grid sensitivity study for the 2D configuration, for $\Delta r = c/48$, $\Delta r = c/96$ and $\Delta r = c/192$. Figure 4 displays the temporal evolution of the aerodynamic force coefficients for the hind airfoil, which are more affected by the vortical interactions. Although not shown here, similar results are obtained for the fore airfoil. It can be appreciated that the temporal history of the forces with $\Delta r = c/96$ is very similar to that of $\Delta r = c/192$, while with $\Delta r = c/48$ the peaks in the forces are clearly different. Moreover, the differences in the propulsive efficiency computed for $\Delta r = c/96$ and $c/192$ are about 3%. Therefore, as a compromise between accuracy and computational cost, all simulations are performed with a grid spacing of $\Delta r = c/96$ in the refined region.

The simulations are started in a grid with a lower resolution ($\Delta r = c/56$ in the refined region) during the first 3 cycles, then the flow field is interpolated on the finer grid and the simulation is restarted and run until convergence is achieved. This entails about $3 - 4$ additional cycles. For the present cases, convergence means that periodic flow conditions are obtained for all cases, with the same period of oscillation of the forcing motion. Consequently, the aerodynamic forces and the flow in the region of interest are periodic, and the discussion of the results is based on the last computed cycle without any loss of generality.

2.3 Definition of aerodynamic coefficients

The aerodynamic force coefficients are defined as

$$C_{k,i} = \frac{2\mathbf{F}_i \cdot \mathbf{e}_k}{\rho U^2 bc}, \tag{4}$$

where $\mathbf{F}_i$ is the total aerodynamic force on the i-wing, $\mathbf{e}_k$ is the unitary vector parallel to the k-axis and ρ is the fluid density. On the other hand, we also analyse sectional forces at a given spanwise position. To that end, we define the sectional force coefficients as

$$c_{k,i}(\xi) = \frac{2\mathbf{f}_i(\xi) \cdot \mathbf{e}_k}{\rho U^2 c}, \tag{5}$$

where $\mathbf{f}_i(\xi)$ is the sectional force at the spanwise position ξ of the i-wing. Note that eq. (5) also corresponds to the aerodynamic force coefficient for the 2D case.

As reported by Lee *et al.* [31], immersed boundary methods generate low amplitude, high frequency spurious oscillations on the forces when the bodies are moving. These oscillations do not affect the statistics of the forces during a cycle, and, since they do not represent a physical phenomenon, are removed in the present analysis using a sharp cut-off low-pass filter. The cutoff frequency is $f_c = (84\Delta t)^{-1} = 50f$, ensuring that only the spurious oscillations are supressed.

Finally, the performance of the wings is assessed by means of the individual propulsive efficiency and the global propulsive efficiency, computed as:

$$\eta_{p,i} = \frac{\overline{C}_{T,i}}{\overline{P}_i}, \qquad\qquad \eta_p = \frac{\sum_{i=1,2} \overline{C}_{T,i}}{\sum_{i=1,2} \overline{P}_i},$$

respectively, where $\overline{C}_{T,i}$ is the average thrust coefficient (computed as the average of $-C_{x,i}$ over a cycle), and $\overline{P}_i$ is the averaged non-dimensional input power of the i wing over a cycle. The instantaneous power is computed as:

$$P_i(t) = C_{z,i}\frac{\dot{h}_i(t)}{U} + \frac{2\mathbf{M}_i \cdot \boldsymbol{\varpi}(t)}{\rho U^3 bc^2}, \tag{6}$$

where $\boldsymbol{\varpi}(t) = \dot{\phi}(t)\mathbf{e}_x + \dot{\theta}(t)\mathbf{e}_\xi$ is the angular frequency. In heaving, $\mathbf{M}_i$ is the aerodynamic moment computed at any point along the ξ_i axis and $\dot{\phi} = 0$. In flapping, $\mathbf{M}_i$ is computed at the intersection of the ξ_i axis with the flapping axis, where $\dot{h} = 0$, so that the first term of eq. (6) is dropped.

3 Results

3.1 2D simulation: reference case

As a reference case we have selected a flow configuration with optimal kinematics as reported in previous works [18]. The temporal evolution of the force coefficients of the 2D reference case is displayed in Figure 5. These results are discussed below together with the results of the 3D simulations. Note that, the force coefficients obtained in the present simulations are in good agreement with the force reported in [18] (not shown). Table 2 gathers the thrust and propulsive efficiencies of each airfoil averaged over a cycle. The motion of the airfoils results in a net production of thrust, with an overall propulsive efficiency slightly larger than the corresponding efficiency of an isolated airfoil oscillating as the fore-airfoil. The average thrust of the hind-wing ($\overline{c}_{T,2}$) is reduced compared to the average thrust of the fore-wing ($\overline{c}_{T,1}$) by approximately 20%. Despite this thrust reduction, the propulsive efficiency of the hind-foil ($\eta_{p,2}$) is very similar to the propulsive efficiency of the fore-wing ($\eta_{p,1}$), as shown in Table 2. Hence, the thrust reduction is accompanied by a reduction of the required power, leading to a relatively constant propulsive efficiency for both airfoils.

Although the motion of the airfoils is symmetric with respect to the horizontal plane, a net lift ($\overline{c}_z = 0.51$) is obtained in the tandem configuration as a result of wake deflection (see Fig. 6a below). This phenomenon does not occur for the isolated airfoil with the present kinematics [18], although it has been observed on isolated airfoils with different motions [32].

$\bar{c}_{T,1}$	$\bar{c}_{T,2}$	$\eta_{p,1}$	$\eta_{p,2}$	η_p
1.02	0.81	0.24	0.23	0.23

Table 2. Averaged results of the 2D simulations. Mean thrust ($\bar{c}_{T,i}$), individual propulsive efficiencies ($\eta_{p,i}$) and global propulsive efficiency (η_p).
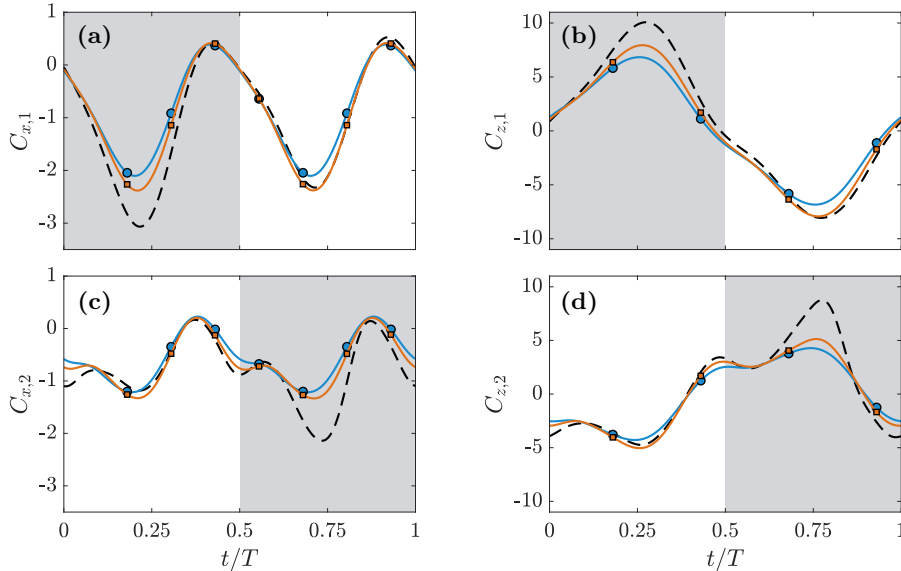

Figure 5. Temporal evolution of the force coefficients. (a-b) Fore-wing, (c-d) hind-wing. (a) and (c) horizontal force coefficient; (b) and (d) vertical force coefficient. (- - -) 2D reference case; (—•—) $A\!\!R = 2$; (—■—) $A\!\!R = 4$. In all plots, the shaded region corresponds to the downstroke of each wing.

3.2 3D simulations: Aspect ratio effects

In order to assess the three dimensional effects due to the finite aspect ratio of the wings, the 2D and the 3D heaving cases are compared first.

Figure 5 depicts the aerodynamic force coefficients ($C_{x,i}$ and $C_{z,i}$) in heaving motion for both $A\!\!R$, together with the forces of the 2D reference case. Qualitatively, the aerodynamic forces of the finite wings are similar to those of the 2D case. Both the fore and the hind-wing produce thrust (i.e., negative horizontal force) during most of the cycle. Figure 5a shows two thrust peaks for the fore-wing at mid-downstroke and mid-upstroke; these peaks are also present for the hind-wing (Figure 5c) but less intense, due to flow interaction, as it will be discussed below. On the other hand, the vertical force for both airfoils is mostly positive during the downstroke and negative during the upstroke (Figures 5b and 5d). These forces yield a zero mean lift, contrary to the non-zero mean lift observed in the 2D case. This difference on the mean lift is clearly observable in the structure of the far wake of these cases. To illustrate this, Figure 6 shows the vertical velocity component time-averaged over a cycle. In the 2D case, Figure 6a, the deflection of the wake with respect to the horizontal plane is clearly visible. In the 3D heaving case with $A\!\!R=4$, no significant deviation from anti-symmetry is observed in the wake, Figure 6b. A similar observation was reported by Dong *et al.* [33] on single plunging foils and wings at similar reduced frequencies.

Regarding the effect of the aspect ratio on the forces, Figures 5a and 5b show that, on the fore-wing, larger $A\!\!R$ leads to higher forces during the mid-upstroke and mid-downstroke. On the hind-wing (Figures 5c and 5d), the temporal evolution of the force coefficients presents more oscillations due to the interaction with the wake of the fore-wing, like in the 2D configuration [18]. Despite this, a qualitatively similar increase in the peak forces of the hind-wing with $A\!\!R$ is also observed. In fact, the average forces over half cycle of each wing decrease roughly 10% from $A\!\!R = 4$ to 2. This is reported in Table 3 that gathers the thrust and lift coefficients averaged over half a cycle and the propulsive efficiencies of each wing.

Figure 7 shows visualizations of the three-dimensional simulations for the cases $A\!\!R = 2$ and $A\!\!R = 4$ at various time instants during the cycle. The vortical structures depicted in the figure correspond to iso-surfaces of the second invariant of the velocity gradient tensor, Q [34]. The iso-surfaces of
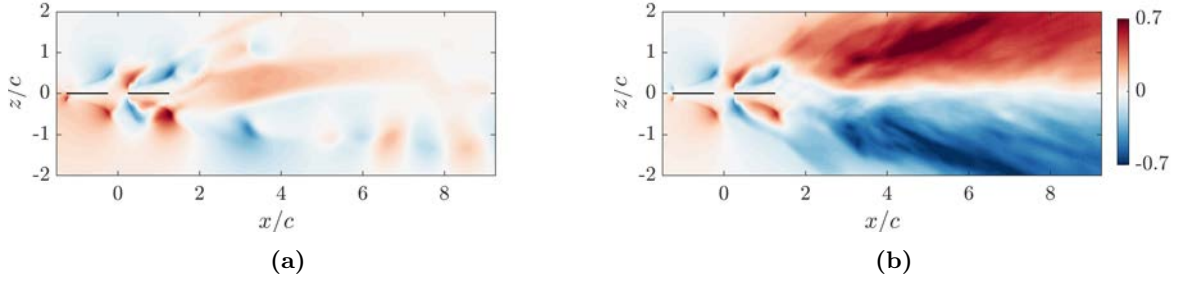
Figure 6. Vertical velocity time-averaged over a cycle. (a) 2D reference case, (b) midspan plane of $AR = 4$ heaving case. Contours are normalized with the freestream velocity, U.

	$\mathcal{R}$	$\overline{C}_{T,1}$	$\overline{C}_{T,2}$	$\overline{C}_{z,1}$	$\overline{C}_{z,2}$	$\eta_{p,1}$	$\eta_{p,2}$	η_p
Heaving	2	0.81	0.57	3.83	2.05	0.23	0.21	0.23
	4	0.91	0.65	4.39	2.24	0.23	0.22	0.23
Flapping	2	0.62	0.45	3.42	1.90	0.22	0.19	0.21
	4	0.66	0.49	3.78	2.04	0.21	0.19	0.20

**Table 3.** Average forces during half-stroke and propulsive efficiencies for the finite span cases.

$Q = 6\Omega_0^2$ are coloured with the spanwise vorticity, ω_y, where $\Omega_0 = 2\pi f$ is the maximum angular velocity. On the other hand, semi-transparent iso-surfaces correspond to $Q = 3\Omega_0^2$ and are associated to less intense vortical structures. Figure 7a depicts the flow structures at the end of the fore-wing's downstroke. For both $\mathcal{R}$ one can appreciate the two main vortical structures developed during the motion, namely: the trailing edge vortex developed by the fore-wing (TV), and a leading edge vortex on the hind-wing. The latter is denoted as the induced leading edge vortex (iLEV), since it is induced by the wake shed by the fore-wing. For both $\mathcal{R}$, the TV and the iLEV tilt upwards and break near the tips of the hind-wing. However, for $\mathcal{R} = 4$, there is a region at the midspan where both vortices resemble two-dimensional vortices. This breakdown observed near the wing tips progresses towards mid section, as observed at later time instants in Figures 7b and 7c. The progression of the breakdown seems to occur at the same velocity for both $\mathcal{R}$. As a consequence, the dipole in the midspan section of the $\mathcal{R} = 2$ case breaks down earlier than in the $\mathcal{R} = 4$ case. This breakdown of the vortices at the midspan is in accordance with observations on pitching tandem wings of $\mathcal{R} = 2$ [21]. Finally, it is interesting to note that the vortex structures near the tips of both wings are very similar for both $\mathcal{R}$ at all times depicted in Figure 7.

It is interesting to analyse if the differences between the flow structures observed in Figure 7 for each $\mathcal{R}$ have a direct impact on the forces. Hence, we compute the sectional forces at the mid-span section, $\xi = \xi_m$ (see Figures 2c and 2d) and at the inboard (or equivalently, outboard) sections, $\xi = \xi_I (\xi_O)$. These sectional force coefficients are shown in Figure 8. The sectional force coefficients differ at the mid-span (Figure 8a), where Figure 7a shows differences in the vortical structures of cases $\mathcal{R} = 2$ and 4. In particular, Figure 8a shows that the peak sectional forces of both wing at midspan decrease with decreasing $\mathcal{R}$. On the other hand, Figure 8b shows that the sectional forces at spanwise positions which are influenced by the wing-tip vortices are very similar for both $\mathcal{R}$, provided that sections at the same distance to the wing tip are considered. Comparison of sectional forces at different chordwise sections reveals that, for the present case, this similarity is extended up to $0.75c$ from the wing tips for both the fore-wing and the hind-wing (not shown).

In order to analyse the origin of the discrepancies in the forces at the midspan section, Figures 9 and 10 depict the spanwise vorticity of the 2D case, and of the 3D simulations at $\xi = \xi_m$, respectively. Figure 9 shows a complete cycle of the 2D case. It is interesting to compare the first half (Figures 9a–9d), which corresponds to the downstroke of the fore-wing, and the second half of the cycle (Figures 9e–9h). One can appreciate that the dipole that is formed by the TV and the iLEV on the lower surface of the hind-airfoil during its upstroke (Figures 9a–9c) remains close to the hind-airfoil during its downstroke (Figures 9d–9f). The same does not happen to the dipole that develops on the upper surface (Figures 9e and 9f), which detaches from the foil and travels downstream (Figures 9g and 9h). This difference is clearly appreciated by analysing the position of the vortices in Figures 9a and 9f. The relative attachment of the dipole during the hind-wing downstroke explains the larger peak forces near $t/T = 0.75$ (Figure 9f) compared to those at $t/T = 0.25$ (Figure 9b), during the upstroke of the
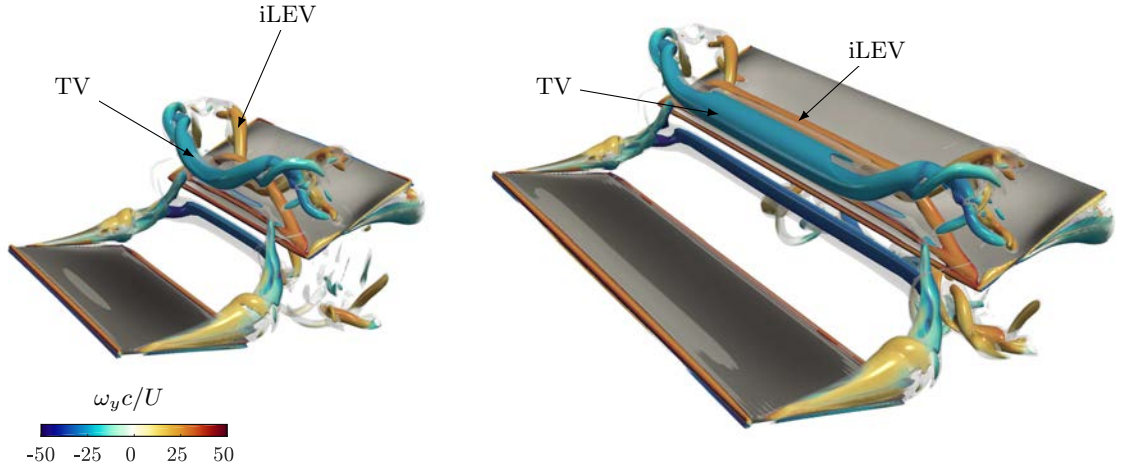
(a) $t/T = 0.5$
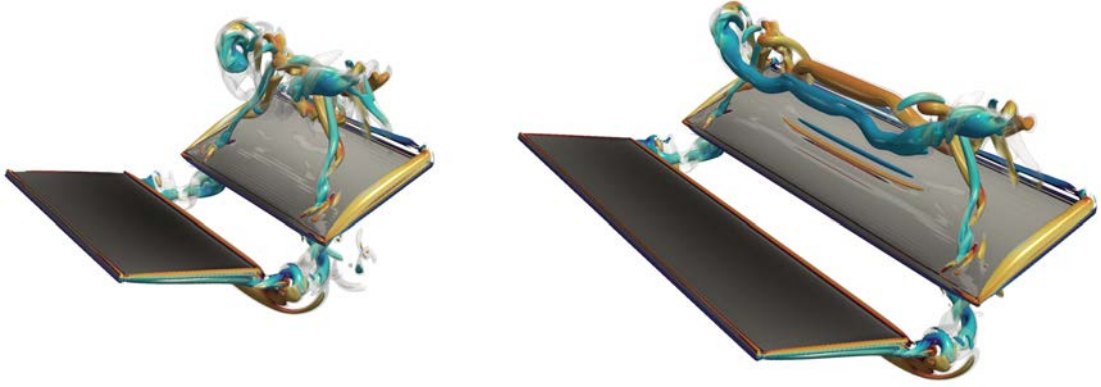
(b) $t/T = 0.75$
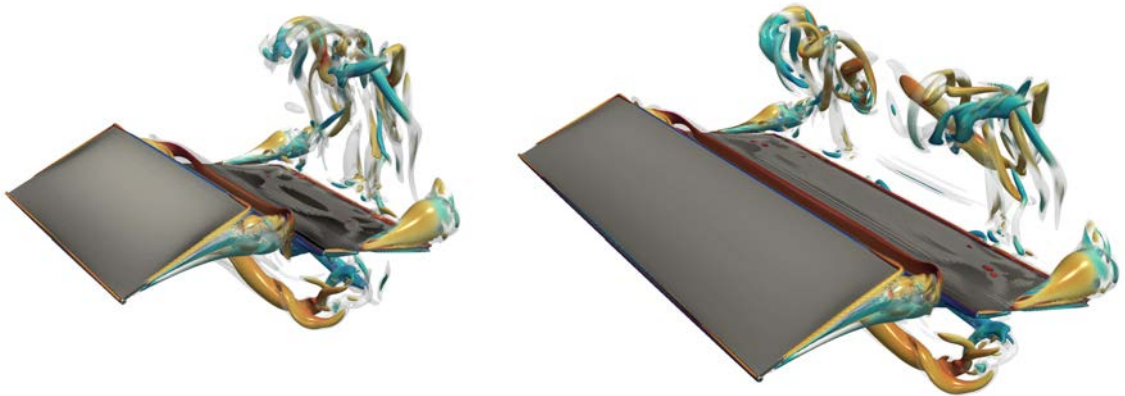
(c) $t/T = 1$

Figure 7. Flow visualization of the cases in heaving motion at various time instants: (a) end of the fore-wing downstroke; (b) fore-wing mid-upstroke; and (c) end of the fore-wing upstroke. (left) $A\!\!R = 2$, and (right) $A\!\!R = 4$. Vortices are represented by means of the Q-criterion [34]. Semi-transparent iso-surface correspond to $Q = 3\Omega_0^2$; iso-surface coloured with the spanwise vorticity, ω_y, correspond to $Q = 6\Omega_0^2$.
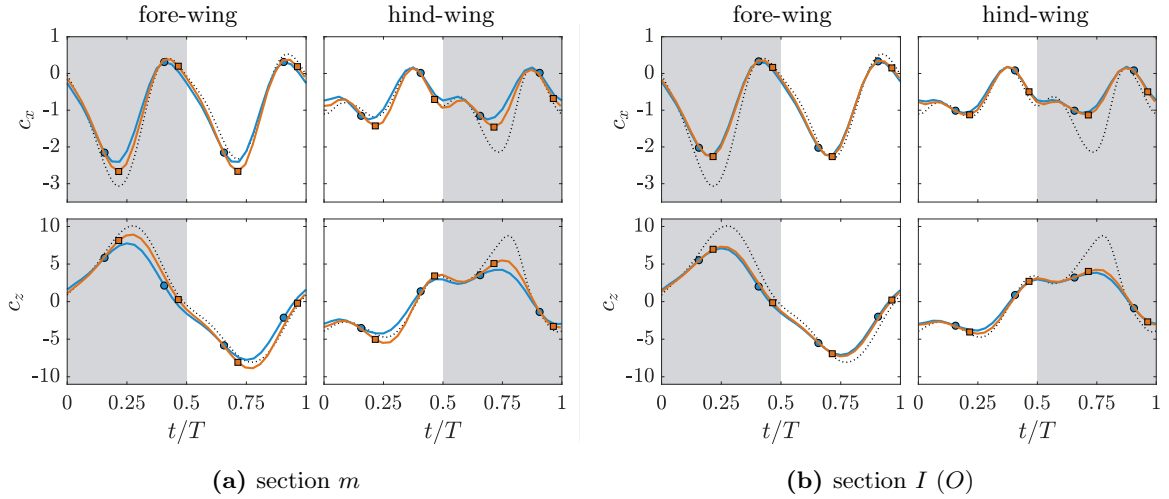
(a) section m **(b)** section I (O)

Figure 8. Temporal evolution of sectional force coefficients at chordwise sections (a) $\xi = \xi_m$ and (b) $\xi = \xi_I$. (—•—) $Æ = 2$, (—■—) $Æ = 4$ and (········) 2D force coefficient. As in Figure 5, the shaded region correspond to the downstroke of each wing.
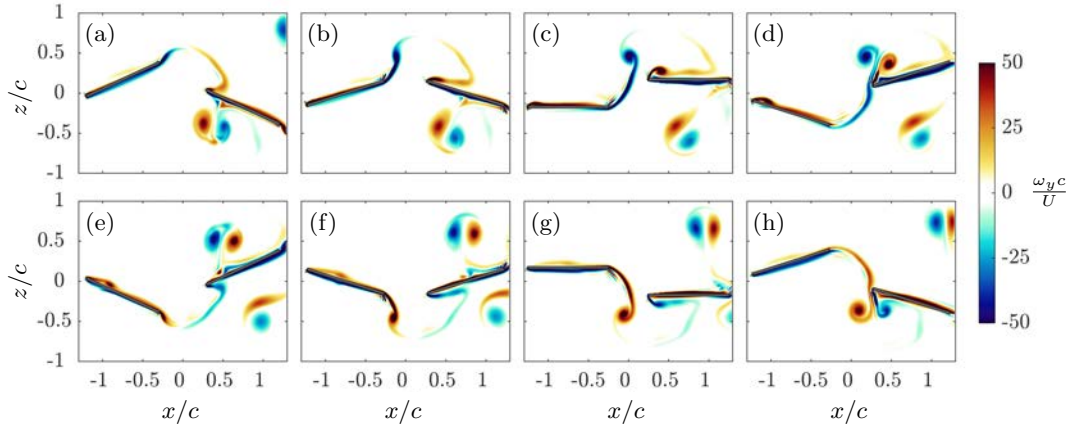

Figure 9. Spanwise vorticity contours of the 2D simulation during a full period. Pictures correspond to different equidistant time instants. (a-d) from $t/T = 0.125$ to $t/T = 0.5$; (e-h): from $t/T = 0.625$ to $t/T = 1$.

hind-wing, as shown in Figure 5. Likewise, the development of a leading edge vortex on the suction surface of the fore-wing at the end of its downstroke (Figure 9d) explains the force reduction during its upstroke. In particular, this vortex lowers the pressure on the upper surface, leading to an increase in the force normal to the airfoil whose projection on the x- and z-axes leads to an increase of both c_x (thrust reduction) and c_z (negative force reduction), respectively.

Figure 10 displays only the first half of the cycle for the finite aspect ratio wings, since the flow is symmetric with respect to the $z = 0$ plane on the other half of the cycle. The spanwise vorticity contours at the mid-span show that the iLEV development from the shear layer of the fore-wing, as well as its first interaction with the TV, are qualitatively similar to the 2D case (Figures 9a–9d) for both $Æ$. The subsequent evolution of the dipole can be observed on the lower surface of the hind-wing, which corresponds to the vortices shed during the previous cycle. Specifically, the vortical structures on the lower hind-wing surface would correspond to the iLEV and TV at $t = t_0 + 0.5T$ (being t_0 the time specified in Figure 10) with the opposite vorticity. It is observed that, as the vortices interact and travel downstream, the differences between the cases become more evident. For $Æ = 4$ (Figures 10e–10h), the dipole travels downstream and detaches from the hind-wing, like during the downstroke of the 2D hind-airfoil (Figures 9e–9h). On the contrary, the vorticity intensity of the dipole for $Æ = 4$ diminishes faster than its 2D counterpart. This effect is due to the *spanwise compression* of the wake, also observed for single pitching/heaving wings [33, 35, 36, 37]. On the other hand, a proper dipole is not formed between the TV and the iLEV over the $Æ = 2$ hind-wing (Figures 10a–10d); instead, vortex breakdown from the tips reach the midspan section before, as shown in Figure 7b.
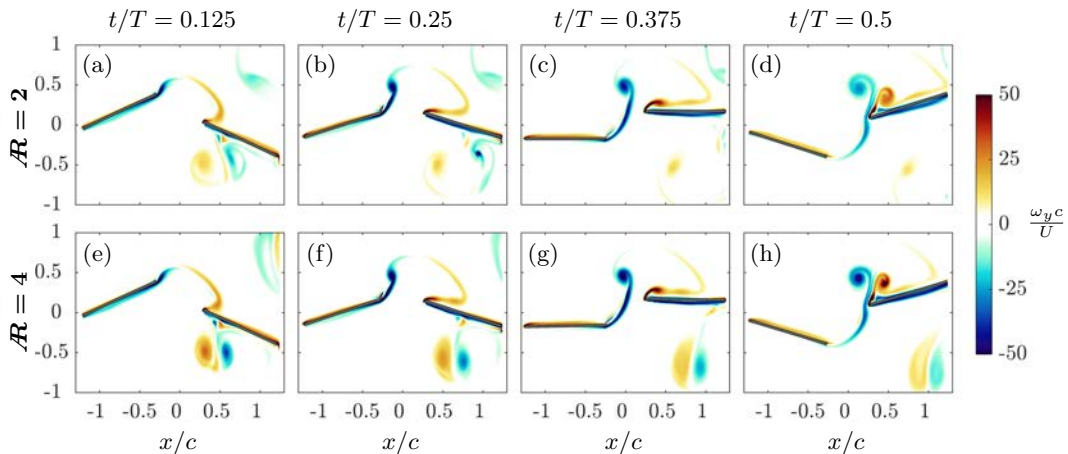
Figure 10. Spanwise vorticity contours at section $\xi = \xi_m$ during the downstroke of the fore-wing. From left to right, $t/T = 0.125, 0.25, 0.375$ and 0.5. The upper row corresponds to $\mathcal{R} = 2$ and the lower row to $\mathcal{R} = 4$.

Although vortical interaction is clearly different at midspan of the hind-wing for $\mathcal{R} = 2$ and 4, it does not explain the differences of the sectional forces on the fore-wing (Figure 8a), since no vortices are found at the midspan of the fore-wing. Hence, the reduction of the sectional forces at $\xi = \xi_m$ on the fore-wing with lower $\mathcal{R}$ seems more likely explained by finite-wing effects, namely, downwash induced velocity as in steady aerodynamics. Moreover, since the difference of the sectional force of the hind-wing with $\mathcal{R}$ is similar to that of the fore-wing, it can be concluded that finite-wing effects are also the main responsible for force reduction on the hind-wing when $\mathcal{R}$ decreases. Consequently, vortex breakdown at the midspan has a secondary effect on the forces since it does not occur close to the wing surface [24].

To summarize, Table 3 gathers, for each wing, the thrust and lift coefficients averaged over half a cycle, as well as the individual and global propulsive efficiencies. The averaged force coefficients are found to be smaller for $\mathcal{R} = 2$ compared to $\mathcal{R} = 4$, both for the fore-wing and the hind-wing. If the mean thrust of each wing is compared to its two-dimensional counterpart (Table 2), a reduction of approximately 21% and 11% is obtained for the fore-wing of $\mathcal{R} = 2$ and 4, respectively. Preliminary simulations of isolated wings (not shown here) have shown that the thrust generated by the fore-wing is independent of the vortical interaction between the fore- and hind-wings, in agreement with previous works [8, 16]. This suggests that the aforementioned thrust reduction is mainly due to wing-tip effects, namely, induced downwash velocity. For the hind-wing, the thrust reduction from 2D to 3D is larger, from 29% for $\mathcal{R} = 2$ to 20% for $\mathcal{R} = 4$ wings. Consequently, three-dimensional vortical mechanisms which are not present in the 2D case (i.e., wing-tip vortices and vortex breakdown) influence the hind-wing's thrust generation. Indeed, the thrust reduction of the hind-wing with respect to the fore-wing $(1 - \overline{C}_{T,2}/\overline{C}_{T,1})$ is very similar for both aspect ratios (30% and 28% for $\mathcal{R} = 2$ and 4, respectively), and higher than for the two-dimensional case, which is close to 20%. This leads to the conclusion that 3D vortex interaction, for the $\mathcal{R}$ considered in this study, has a non-negligible impact on the aerodynamic forces. Despite the detriment in thrust generation, the propulsive efficiency of the hind-wing $(\eta_{p,2})$ is very similar to the propulsive efficiency of the fore-wing $(\eta_{p,1})$ and only slightly lower than the individual propulsive efficiencies of the two-dimensional case. Consequently, the overall propulsive efficiency, η_p is virtually the same. The low dependency of η_p on $\mathcal{R}$ was reported by Dong et al. [33] for single wings in pitching and heaving motion, and later by Buchholz & Smits [37] for a low-$\mathcal{R}$ pitching wing. In both cases, the Strouhal number was in the same range as the one considered in the present study.

3.3 3D simulations: Heaving vs. flapping

From a mechanical point of view, heaving is not a realistic motion for either MAVs or flying animals. Therefore, in the present section we analyse the differences between a pair of tandem finite wings in heaving (section 3.2) and the same wings performing a flapping motion about a fixed axis, as described in section 2.

Figure 11 shows the temporal evolution of the aerodynamic force coefficients in the heaving and flapping configurations, for both $\mathcal{R} = 2$ and 4. In the flapping case, for both the fore- and the
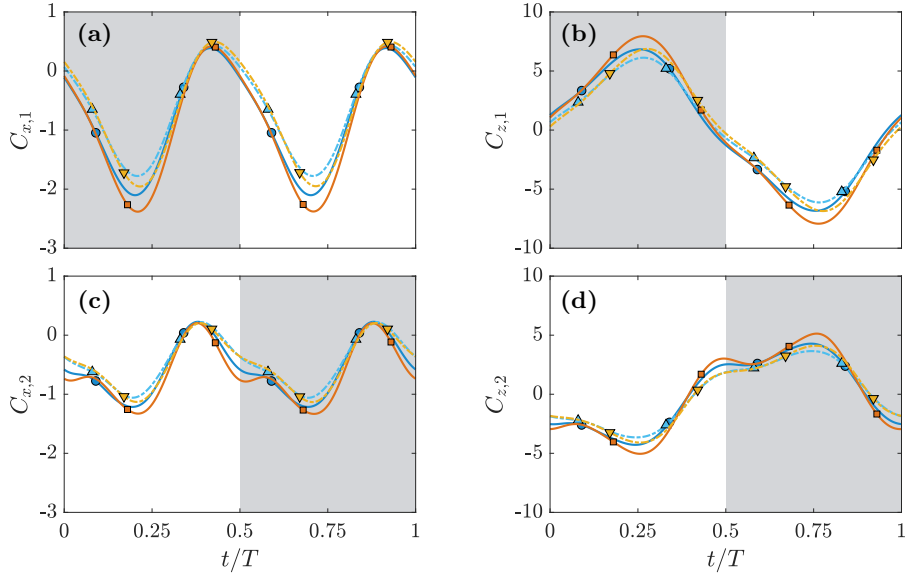
Figure 11. Temporal evolution of the force coefficients. (a-b) Fore-wing, (c-d) hind-wing. (a) and (c) horizontal force coefficient; (b) and (d) vertical force coefficient. $\mathcal{R} = 2$: ($-\bullet-$) heaving, ($-\triangle-$) flapping; and $\mathcal{R} = 4$ ($-\blacksquare-$) heaving, ($-\triangledown-$) flapping.

hind-wing, a decrease of the thrust peaks is observed compared to to the heaving case (Figures 11a and 11c), while drag peaks (at $t/T \approx 0.35$ and 0.85) remain virtually equal. This decrease is more pronounced for $\mathcal{R} = 4$ than for $\mathcal{R} = 2$. As a consequence, the average thrust of both wings is reduced in flapping motion when compared to heaving motion (see Table 3). Regarding the effect on the vertical force, Figures 11b and 11d reveal an amplitude decrease for both wings in the flapping case. Moreover, from heaving to flapping, there is a shift in the time at which forces are maximum.

Top row of Figure 12 shows the sectional aerodynamic forces at the characteristic section, ξ_C (viz., the section which moves like the 2D-configuration in flapping motion) for both $\mathcal{R}$ and for the heaving and flapping motion. One can appreciate that, for a given $\mathcal{R}$, the sectional forces at ξ_C are very similar both in heaving and flapping. This observation holds for the fore and the hind-wing and for the horizontal and vertical components of the forces. However, the sectional force coefficients vary with $\mathcal{R}$. In particular, the peak forces are diminished for the lower aspect ratio. Since the characteristic section, ξ_C, changes with $\mathcal{R}$ ($\xi_C = 1.3c$ for $\mathcal{R} = 2$, and $\xi_C = 2.6$ for $\mathcal{R} = 4$), the fact that the sectional forces at ξ_C vary with $\mathcal{R}$ but not with the motion seems to suggest that the sectional forces do not depend only on the sectional motion but also on the vortical structures.

Since the amplitude of the aerodynamic forces is lower in flapping motion, there must be wing sections with lower sectional forces than at ξ_C. To show this, Figure 12 (bottom row) displays the sectional forces at ξ_I and ξ_O for the flapping motion of the $\mathcal{R} = 2$ and 4 wings. As expected, the amplitude of the vertical force is decreased at the inboard sections of the wings; the same happens for the peak thrust. The opposite behaviour is observed at outboard wing section. Moreover, it is interesting to note that, in addition to a reduction of the peak thrust at inboard sections, there is an increase of positive horizontal force (drag), at the end of the downstroke. This effect is more pronounced for the $\mathcal{R} = 4$ wing. Additionally, the peak of the forces shifts forward in time from outboard to inboard wing sections. This shift is related to the spanwise variation of the *effective angle of attack*, $\alpha_i(\xi)$, which is the angle between the chordwise direction (τ_i in Figure 2) and the flow velocity at the mid-chord of the ξ_i-section. Particularly,

$$\alpha_i(\xi) = \theta_i - \tan^{-1}\left(\frac{\dot{\phi}_i(\Delta\xi + \xi)}{U}\right) \tag{7}$$

where $\dot{\phi}$ is the time derivative of ϕ. The peak of α_i occurs earlier at outboard sections than at inboard sections of the wing, in accordance to peak of the forces.

The spanwise variation of the forces for both wings can be understood by looking at the spanwise vorticity (Figure 13). The results correspond to $\mathcal{R} = 4$, since for this case the differences between the outboard and the inboard sections are more noticeable. Figure 13 depicts, for the inboard (ξ_I),
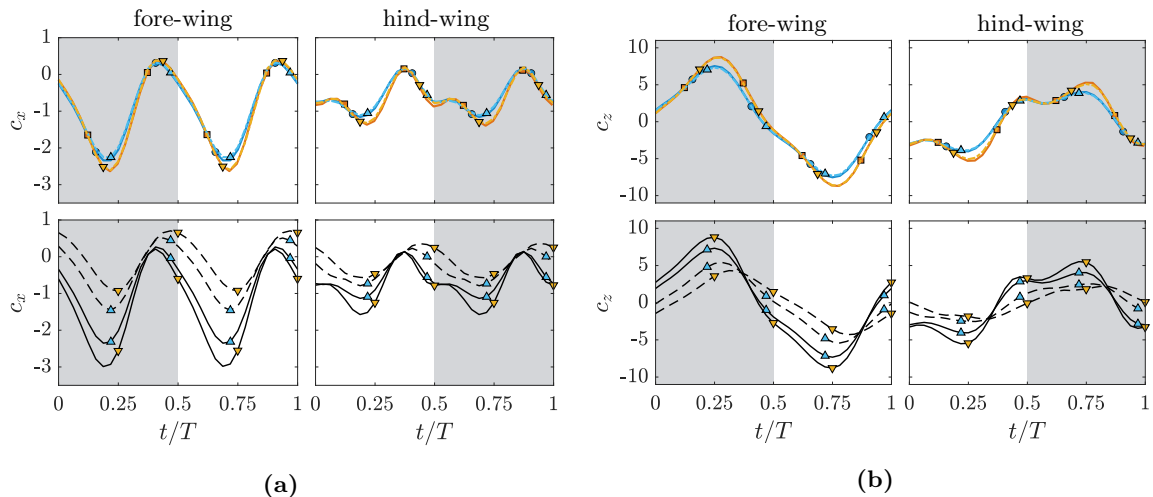
12

Figure 12. Temporal evolution of the sectional (a) horizontal and (b) vertical force coefficients. For both figures, top row displays the sectional forces at the characteristic section, $\xi_C = 0.65b$: $\mathit{AR} = 2$: ($-\bullet-$) heaving, ($-\triangle-$) flapping; $\mathit{AR} = 4$: ($-\blacksquare-$) heaving, ($-\triangledown-$) flapping. Bottom row displays the sectional forces near the wing tips during flapping motion: ($-$ $-$ $-$) inboard section, ξ_I, and ($\underline{\quad}$) outboard section, ξ_O. ($\triangle$) $\mathit{AR} = 2$ and ($\triangledown$) $\mathit{AR} = 4$.

midspan (ξ_m) and outboard (ξ_O) wing sections, the vorticity normal to the cylindrical surface whose axis of revolution coincides with the flapping axis and with radii equal to $\Delta\xi + \xi_I$, $\Delta\xi + \xi_m$ and $\Delta\xi + \xi_O$, respectively. These surfaces are also illustrated in Figure 14a. It is noticeable that the vorticity at the midspan (second row in Figure 13) is very similar to that in heaving motion at the same section, Figure 10. This is not true for the inboard and outboard wing sections. If we focus on the fore-wing at $\xi = \xi_I$, a vortex is developed on the lower surface of the fore-wing, due to the pitch-up rotation of the wing, $t/T = 0.375$. This vortex is labelled 1 in the figure. During the cycle, this vortex travels downstream until it merges with the shear layer shed at the hind-wing's trailing edge. The vortex motion is chronologically indicated by the numbers in Figure 13 (top row). Note that, since only half a cycle is shown, the vortex flips side from 2 to 3 and from 6 to 7 in the present representation. On the contrary, if we compare the vorticity contour at the inboard (top row of Figure 13) and outboard (bottom row) wing sections, it is appreciated that no vortex is shed at $\xi = \xi_O$. Instead, the shear layer on the upper surface detaches at the leading edge ($t/T = 0.5$).

The spanwise variation of the vorticity can be explained by the spanwise variation of the *effective angle of attack* (see eq. (7)). Near the inboard wing tip, the contribution of the vertical velocity to α_1 is small, and inboard sections behave like an airfoil in pure pitching. Specifically, the shedding and travelling of the vortices at the fore-wing leading edge at ξ_I is similar to that observed in pure pitching foils for $\theta_0 \geq 8°$ (and similar St_c and Re) [38]. Outboard fore-wing sections have larger *heaving* amplitudes. As a consequence, an LEV starts developing after the mid-downstroke ($t/T = 0.375$ in Figure 13) at outboard spanwise locations, in a similar fashion as wings in flapping without pitching motion [27]. However, pitch-up rotation inhibits its later development and shedding as for flapping wings without pitching [27] or heaving airfoils [32].

The spanwise variation of the fore-wing wake flow affects the hind-wing. Figure 13 shows that, for a given time instant, the trailing edge vortex is located further upwards and downstream at outboard spanwise positions. As a consequence, the shear layer of the TV impinges earlier on the leading edge at outboard wing sections and the iLEV starts developing earlier at outboard wing sections. This is illustrated in the last column of Figure 13 ($t/T = 0.5$), where it is observed that the shear layer shed during the downstroke of the fore-wing have just impinged on the leading edge of outboard wing sections (bottom row); meanwhile at the inboard wing sections the shear layer has not yet reached the leading edge of the hind-wing.

Figure 14 shows that, even with the spanwise variation of TV and iLEV, the overall vortical interactions on the hind-wing for the flapping case are similar to the heaving case. Nonetheless, it is observed that, as a consequence of the varying intensity of the vortices along the spanwise direction, both the TV and iLEV are found more downstream and upwards on the outboard regions when compared to the heaving case. At longer times, there is a vortex breakdown similar to the heaving case (Figure 15).

Regarding averaged forces, Table 3 shows that the mean thrust of each wing decreases in the flapping
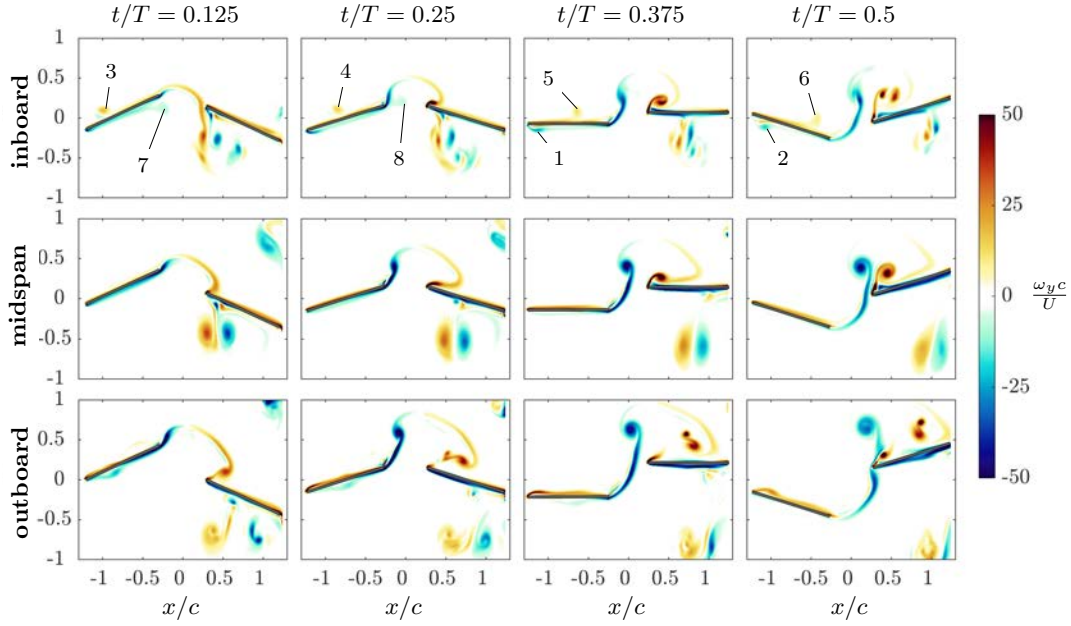
13

Figure 13. Spanwise vorticity contours during the downstroke (upstroke) of the fore- (hind-)wing at different chordwise sections of $Æ = 4$ wings in flapping motion. Each column correspond to a given time: from left to right, $t/T = 0.125$, 0.25, 0.375 and 0.5. Upper row correspond to the inboard wing tip ($\xi = \xi_I$), middle row correspond to the midspan section ($\xi = \xi_m$), and lower row correspond to the outboard wing tip ($\xi = \xi_O$).
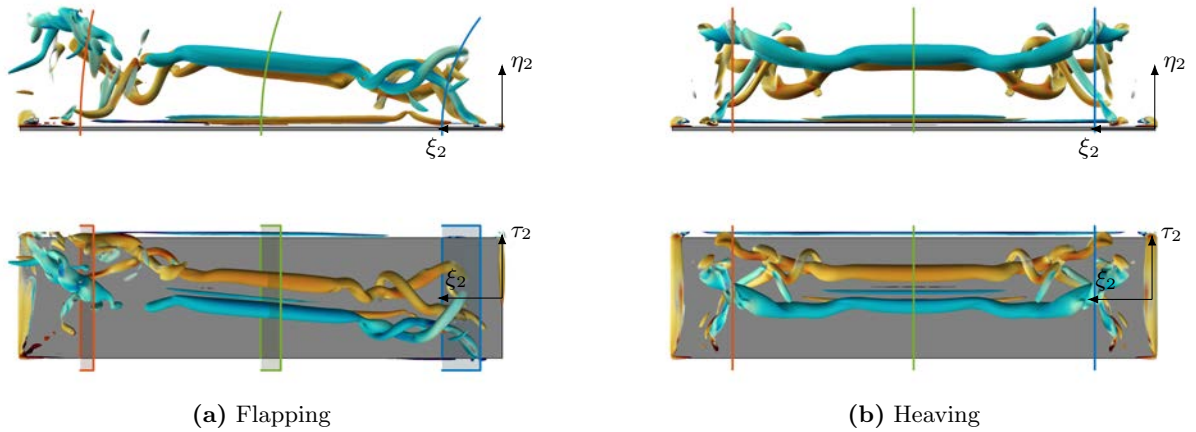

(a) Flapping

(b) Heaving

Figure 14. Vortical structures on the $Æ = 4$ hind-wing at $t/T = 0.75$ for the (a) flapping and (b) heaving case. The vortical structures correspond to $Q = 6\Omega_0^2$ and are coloured with ω_y (legend as in Figure 7). The planes sketched in (a) and (b) are the ones used to display the vorticity contours in Figures 10 and 13, respectively (note that in the latter, inboard and outboard planes are equivalent).
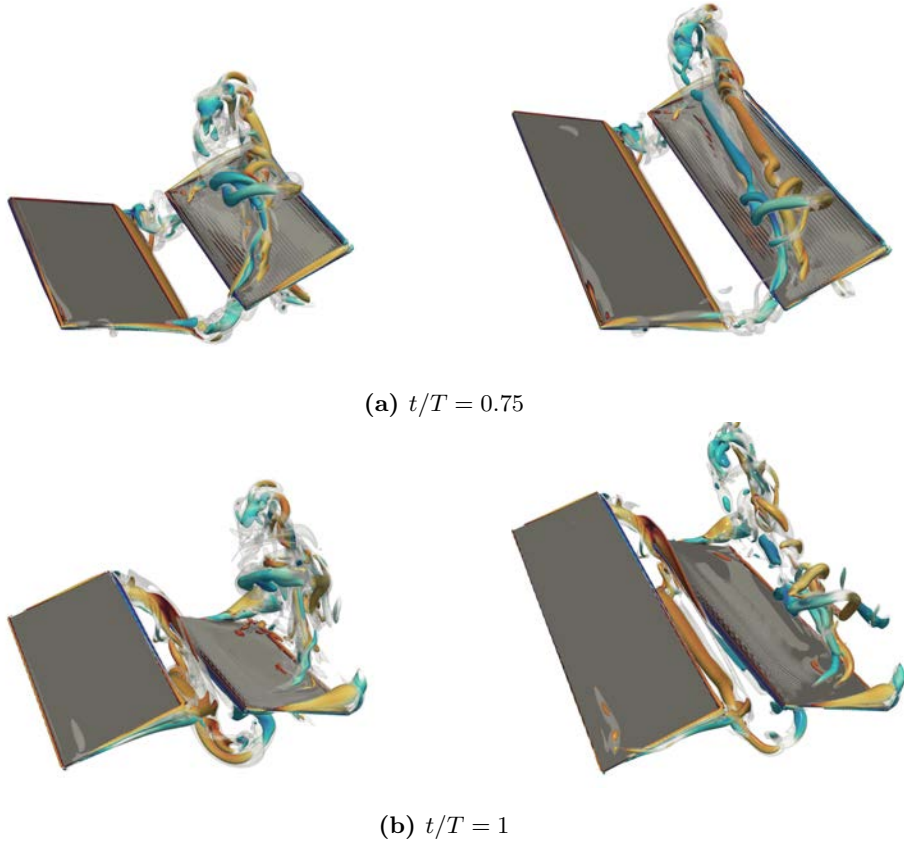
(a) $t/T = 0.75$

(b) $t/T = 1$

Figure 15. Visualization of the cases in flapping motion. (a) $t/T = 0.75$ and (b) $t/T = 1$. The closer tips correspond to the inboard wingtips. Iso-surfaces of the Q-criterion are equal to those on Figure 7.

case compared to the heaving case. The reduction is more pronounced for $\mathcal{R} = 4$ (27% and 26% for the fore- and hind-wing, respectively) than for $\mathcal{R} = 2$ (23% and 20% for the fore- and hind-wing, respectively). On the other hand, the thrust reduction of the hind-wing compared to the fore-wing is 27% for both $\mathcal{R}$, being very similar to the results observed in heaving. This entails that, as shown before, the interaction between both wings is rather similar both in heaving and flapping motions. Finally, a reduction in the propulsive efficiency, η_p, is also observed in the flapping case compared to the heaving case. Contrary to heaving, η_p slightly decreases with $\mathcal{R}$ in the flapping case. This adverse effect of $\mathcal{R}$ can be attributed to the fact that, as $\mathcal{R}$ increases, there is a larger region of the wing which has a *suboptimal* motion, particularly close to the inboard wing tip, whose sectional propulsive efficiency is lower. This is true for both the fore- and the hind-wing.

4 Conclusions

The objective of this study was to analyse how three dimensional effects influence the performance of wings in tandem configuration undergoing a two-dimensional optimal kinematics. To do so, direct numerical simulations, both in 2D and 3D, have been performed.

First, finite aspect ratio effects have been studied by considering wings of two different aspect ratios, 2 and 4, undergoing a heaving and pitching motion corresponding to the 2D optimal kinematics [18]. The analysis has been based on comparisons of the flow structure and of the aerodynamic forces on the wings. For both $\mathcal{R}$, the interaction mechanisms between the fore- and the hind-wing vortical structures are qualitatively similar to the two-dimensional case. Namely, the shear layer shed by the fore-wing induces a leading edge vortex on the hind-wing surface which interacts with the trailing vortex of the fore-wing. However, in 3D, there is a breakdown of both vortices starting at the wing tips of the hind-wing and progressing towards the midspan, leading to somewhat different vortex organisation surrounding the wings. The mean thrust of the finite wings is lower than in the 2D case. This reduction is larger with decreasing $\mathcal{R}$. Moreover, it is found that the thrust reduction is more pronounced on the hind-wing. This entails that 3D vortical mechanisms, not present in 2D, have a non-negligible impact on the aerodynamic forces of the hind-wing. Nonetheless, the propulsive efficiency (η_p) remains approximately constant for both $\mathcal{R}$ and for the 2D dimensional case. Our

results are consistent with the observations of Dong et al [33] for single heaving/pitching wings, as well as those of Broering and Lian [11] for tandem wings at a significantly lower Reynolds number than the one considered here.

The results of the tandem wings in heaving motion have been compared to those obtained for a flapping motion. The objective was to analyse the effects of having a more realistic, three-dimensional motion. The results show that, for a given AR, the aerodynamic forces decrease when the wings are in flapping motion. A comparison of the sectional forces along the span reveals that the forces are nearly identical for the heaving motion at midspan and for the flapping motion at the characteristic section (i.e. the section whose motion corresponds to the 2D airfoil motion). On the contrary, the amplitude of the vertical force decreases at inboard wing sections in flapping motion; likewise, both the amplitude and the mean value of the thrust force decrease. This detrimental behaviour has been linked to a sub-optimal motion of the inboard region, which is close to a pure pitching motion of low efficiency [38]. It should be noted that this behaviour is found both on the fore-wing and on the hind-wing. This sub-optimal region of the wings entails not only a decrease of the mean thrust, but also a decrease of the propulsive efficiency compared to the heaving case, which is more noticeable for $AR = 4$, since the extension of this region is larger in this case.

The present results also suggest that for 3D configurations, a moderate spacing between the wings (i.e, $s \lesssim c$) is probably desirable to avoid the full breakdown of the TEV before it reaches the hind-wing. This is not the case for 2D airfoils in tandem configuration, where the vortices shed by the fore-wing dissipate very slowly, allowing basically the same vortical interactions when the distance between the airfoils is increased by λ (where λ is the wavelength of wake shed by the fore-wing) [39, 21].

To summarise, it has been found that 2D tandem simulations provide reasonable predictions of the propulsive efficiency of finite aspect ratio wings, in the range of Reynolds and Strouhal numbers studied here. On the other hand, mean thrust production of the hind-wing is not properly estimated in 2D simulations, due to differences between 2D and 3D vortical interactions. Concerning the mean lift, it has been observed that a non-zero value is obtained in 2D that can be attributed to the well-known phenomenon of wake deflection. On the contrary, in the 3D simulations the mean lift is zero for all cases. This is consistent with the observations of Dong et al [33] for single heaving/pitching wings and hints that, for finite-aspect ratio tandem wings, the practical relevance of the wake deflection phenomenon might be limited. Finally, it has been found that the aerodynamic performance of the tandem wings is deteriorated when a realistic, three-dimensional flapping motion is considered.

Acknowledgements

References

[1] R. Norberg. *Hovering Flight of the Dragonfly Aeschna Juncea L., Kinematics and Aerodynamics*, pages 763–781. Springer US, 1975.

[2] A. Thomas, G. Taylor, R. Srygley, R. Nudds, and R. Bomphrey. Dragonfly flight: free-flight and tethered flow visualizations reveal a diverse array of unsteady lift-generating mechanisms, controlled primarily via angle of attack. *J. Exp. Biol.*, 207(24):4299–4323, 2004.

[3] D. Alexander. Unusual phase relationships between the forewings and hindwings in flying dragonflies. *J. Exp. Biol.*, 109(1):379–383, 1984.

[4] J. Wakeling and C. Ellington. Dragonfly flight. II. Velocities, accelerations and kinematics of flapping flight. *J. Exp. Biol.*, 200(3):557–582, 1997.

[5] Z. Wang and D. Russell. Effect of forewing and hindwing interactions on aerodynamic forces and power in hovering dragonfly flight. *Phys. Rev. Lett.*, 99:148101, 2007.

[6] F. Lehmann. When wings touch wakes: understanding locomotor force control by wake wing interference in insect wings. *J. Exp. Biol.*, 211(2):224–233, 2007.

[7] J. Usherwood and F. Lehmann. Phasing of dragonfly wings can improve aerodynamic efficiency by removing swirl. *J. R. Soc. Interface*, 5(28):1303–1307, 2008.

[8] W. Maybury and F. Lehmann. The fluid dynamics of flight control by kinematic phase lag variation between two robotic insect wings. *J. Exp. Biol.*, 207(26):4707–4726, 2004.

[9] J. K. Wang and M. Sun. A computational study of the aerodynamics and forewing-hindwing interaction of a model dragonfly in forward flight. *J. Exp. Biol.*, 208(19):3785–3804, 2005.

[10] D. Rival, Schönweitz D., and C. Tropea. Vortex interaction of tandem pitching and plunging plates: a two-dimensional model of hovering dragonfly-like flight. *Bioinspir. Biomim.*, 6(1):016008, 2011.

[11] T. Broering and Y. Lian. Numerical study of tandem flapping wing aerodynamics in both two and three dimensions. *Comput. Fluids*, 115:124–139, 2015.

[12] B. Boschitsch, P. Dewey, and A. Smits. Propulsive performance of unsteady tandem hydrofoils in an in-line configuration. *Phys. Fluids*, 26(5):051901, 2014.

[13] K. Lua, H. Lu, X. Zhang, T. Lim, and K. Yeo. Aerodynamics of two-dimensional flapping wings in tandem configuration. *Phys. Fluids*, 28(12), 2016.

[14] L. Muscutt, G. Weymouth, and B. Ganapathisubramani. Performance augmentation mechanism of in-line tandem flapping foils. *J. Fluid Mech.*, 827:484–505, 2017.

[15] Y. Kamisawa and K. Isogai. Optimum flapping wing motions of dragonfly. *Trans. Japan Soc. Aero. Space Sci.*, 51(172):114–123, 2008.

[16] H. Nagai, K. Fujita, and M. Murozono. Experimental study on forewing–hindwing phasing in hovering and forward flapping flight. *AIAA J.*, 57(9):3779–3790, 2019.

[17] J. Ortega-Casanova and R. Fernandez-Feria. Analysis of the aerodynamic interaction between two plunging plates in tandem at low Reynolds number for maximum propulsive efficiency. *J. Fluids Struct.*, 63:351–373, 2016.

[18] J. Ortega-Casanova and R. Fernández-Feria. Maximum propulsive efficiency of two pitching and plunging plates in tandem at low Reynolds number: A numerical analysis. *Int. J. Numer. Method. Heat Fluid Flow*, 29:4013–4033, 2019.

[19] F. Huera-Huarte. Propulsive performance of a pair of pitching foils in staggered configurations. *J. Fluids Struct.*, 81:1 – 13, 2018.

[20] Y. Zheng, Y. Wu, and H. Tang. An experimental study on the forewing–hindwing interactions in hovering and forward flights. *Int. J. Heat Fluid Flow*, 59:62 – 73, 2016.

[21] M. Kurt and K. Moored. Flow interactions of two- and three-dimensional networked bio-inspired control elements in an in-line arrangement. *Bioinspir. Biomim.*, 13(4):045002, 2018.

[22] M. Sun and S. Lan. A computational study of the aerodynamic forces and power requirements of dragonfly (Aeschna juncea) hovering. *J. Exp. Biol.*, 207(11):1887–1901, 2004.

[23] M. Uhlmann. An immersed boundary method with direct forcing for the simulation of particulate flows. *J. Comput. Phys.*, 209(2):448–476, 2005.

[24] M. Moriche, O. Flores, and M. García-Villalba. On the aerodynamic forces on heaving and pitching airfoils at low Reynolds number. *J. Fluid Mech.*, 828:395–423, 2017.

[25] M. Moriche, M. Raiola, S. Discetti, A. Ianiro, O. Flores, and M. García-Villalba. Assessing aerodynamic force estimation with experiments and simulations of flapping-airfoil flows on the verge of three-dimensionality. *Proc. Inst. Mech. Eng. G J. Aerospace Eng.*, 2019.

[26] M. Moriche, O. Flores, and M. García-Villalba. Three-dimensional instabilities in the wake of a flapping wing at low Reynolds number. *Int. J. Heat Fluid Flow*, 62A:44–55, 2016.

[27] A. Gonzalo, G. Arranz, M. Moriche, M. García-Villalba, and O. Flores. From flapping to heaving: A numerical study of wings in forward flight. *J. Fluids Struct.*, 83:293–309, 2018.

[28] G. Arranz, M. Moriche, M. Uhlmann, O. Flores, and M. García-Villalba. Kinematics and dynamics of the auto-rotation of a model winged seed. *Bioinspir. Biomim.*, 13:036011, 2018.

[29] G. Arranz, A. Gonzalo, M. Uhlmann, O. Flores, and M. García-Villalba. A numerical study of the flow around a model winged seed in auto-rotation. *Flow Turbul. Combust.*, 101(2):477–497, 2018.

[30] M. Moriche, A. Gonzalo, M., O. Flores, and M. García-Villalba. Fast transverse maneuvers at low Reynolds numbers. AIAA 2019-0640, 2019.

[31] J. Lee, J. Kim, Choi H., and K. Yang. Sources of spurious force oscillations from an immersed boundary method for moving-body problems. *J. Comput. Phys.*, 230(7):2677 – 2695, 2011.

[32] G. C. Lewin and H. Haj-Hariri. Modelling thrust generation of a two-dimensional heaving airfoil in a viscous flow. *J. Fluid Mech.*, 492:339–362, 2003.

[33] H. Dong, R. Mittal, and F. M. Najjar. Wake topology and hydrodynamic performance of low-aspect-ratio flapping foils. *J. Fluid Mech.*, 566:309–343, 2006.

[34] J. C. R. Hunt, A. A. Wray, and P. Moin. Eddies, stream, and convergence zones in turbulent flows. *Center For Turbulence Research*, Report CTR-S88, 1988.

[35] J. Buchholz and A. J. Smits. On the evolution of the wake structure produced by a low-aspect-ratio pitching panel. *J. Fluid Mech.*, 546:433–443, 2006.

[36] M. Green, C. Rowley, and A. Smits. The unsteady three-dimensional wake produced by a trapezoidal pitching panel. *J. Fluid Mech.*, 685:117–145, 2011.

[37] J. Buchholz and A. Smits. The wake structure and thrust performance of a rigid low-aspect-ratio pitching panel. *J. Fluid Mech.*, 603:331–365, 2008.

[38] A. Das, R. Shukla, and R. Govardhan. Existence of a sharp transition in the peak propulsive efficiency of a low-*Re* pitching foil. *J. Fluid Mech.*, 800:307–326, 2016.

[39] X. Zhu, G. He, and X. Zhang. Flow-mediated interactions between two self-propelled flapping filaments in tandem configuration. *Phys. Rev. Lett.*, 113:238105, Dec 2014.